Extreme Mechanics Letters 21 (2018) 76–81

Contents lists available at ScienceDirect

Extreme Mechanics Letters

journal homepage: www.elsevier.com/locate/eml

On the realization of a second buckling mode in a periodically-constrained heavy elastica

Diego F. Muriel *, Edwin A. Cowen

DeFrees Hydraulics Laboratory, School of Civil and Environmental Engineering, Cornell University, Ithaca, NY 14853, USA

ARTICLE INFO

Article history:
Received 27 February 2018
Received in revised form 28 March 2018
Accepted 29 March 2018
Available online 8 April 2018

Keywords:
Heavy elastica
Buckling
Elastic instability
Elastica

ABSTRACT

Structural instabilities are often considered a failure state and therefore engineers are trained to avoid them. Recently, flexible buckled structures have gone from merely describing a phenomenon (e.g., twisting of vines, DNA mechanics), to being exploited for novel functionalities (e.g., stretchable electronics, energy harvesting). Herein we present results from a study of the static deformation of a periodically-constrained plate proposed by Muriel et al. (2016) as a hydrokinetic energy harvester. Experimentally, a polycarbonate sheet is placed under longitudinal compression with external forcing provided by equally spaced tension lines anchored in a frame, inducing a second mode wave-like deformation. No additional constraints are placed on the material. To predict this deformation, we proposed a model based on the two-dimensional heavy elastica, where the dependence of the distributed weight to the curvature prevents a closed form solution. Therefore, we solve numerically the nonlinear system of equations of an elemental strip, with the assumptions of uniform cross-section, elasticity, and density, and consider only cylindrical bending and the plate to be thin enough such that the Euler assumption holds. Tension lines are treated with a constitutive equation consistent with Hook's law, and contact points between lines and the plate are considered as passive (i.e., no friction, no moment, and no elastic singularity). The system is discretized using a second-order centered difference scheme, and solved using trust-region and Levenberg–Marquardt algorithms. The numerical solutions predict the deformation well and confirm the experimental finding of elastic bifurcation (solutions of second mode deformations), buckling instability, and points towards the possibility of deformations resembling higher order modes not seen in the experiments. The sensitivity of the constitutive relation to small strain variations poses questions about convergence of such higher order modes. This structural model is the first step towards a fully coupled fluid–structure model of a deformation that shows promise on reducing the external forcing needed to start structural oscillations.

1. On the functionality of buckled structures

Buckling of slender structures is a phenomenon with widespread applications. Its study has evolved from Euler [1] and the double-pinned elastica, to more complex applications such as buckling of metabeams [2], folding of sheet-like tissues [3], coiled tubing in industry [4–6], folding of sheets over fluids [7,8], mechanics of DNA [9], and nanoribbons and nanowires [10,11]. A common theme among these studies, is the fact that the geometry is the main factor contributing to nonlinearities (material, force/displacement boundary conditions are also possible sources).

Despite buckling instabilities being traditionally considered a failure state, there are multiple studies exploiting such structural instabilities for new applications [12]. Some examples are stretchable electronics [13,14], adaptive flow control [15], drag control [16], and energy harvesting [17–24]. Closed form solutions to these problems are restricted to simple problems [25], and therefore, analysis often turn to Hamiltonian formulations to obtain equilibrium equations.

In the context of energy harvesting, one class of devices exploit the oscillatory behavior of slender flexible structures excited by ambient vibrations or fluid forcing. On the latter, a structure transitions from an equilibrium state to an oscillatory behavior together with the onset of flow instabilities. This so called flapping instability relies on the ability of the flow to reach a critical velocity at which structural oscillatory behavior starts. In short, it is a phenomenon that involves the interaction of a fluid's hydrodynamic pressure and drag forces, and the structure's elastic, inertial, and damping forces [26,27].

Muriel et al. [30], Muriel and Cowen [31] presented a structure that did not relay on both flow instabilities and structural

* Corresponding author.
E-mail addresses: dfm99@cornell.edu (D.F. Muriel), eac20@cornell.edu (E.A. Cowen).

https://doi.org/10.1016/j.eml.2018.03.006
2352-4316/

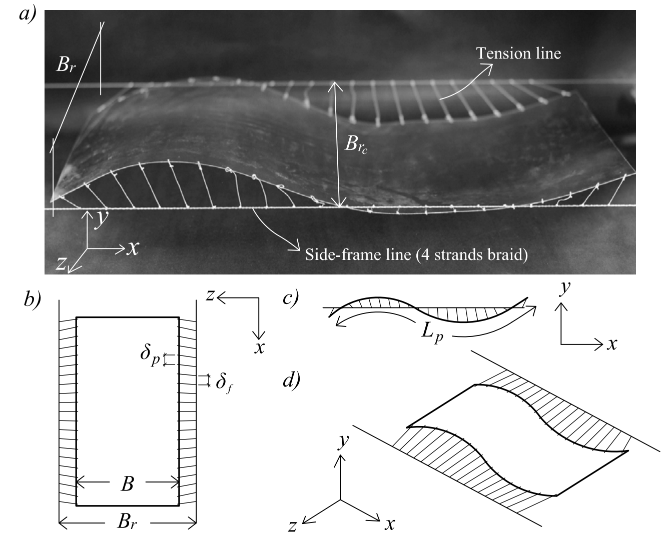

Fig. 1. (a) Experimental realization of a second mode deformation on a translucent polycarbonate sheet: separation between side-frame lines, B_r, and between side-frame lines at $^1/_2$, B_{r_c}. (b) Top view: plate's width, B, separation between inner tension lines in the device, δ_p, and in the frame, δ_f; (b) Side view: plate's length, L_p; (c) Isometric projection.
Source: (b) to (c) are adapted from [28,29].

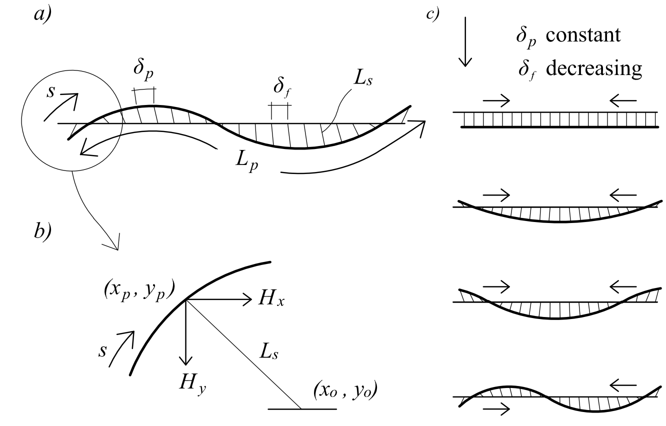

Fig. 2. Buckled plate projections onto a two-dimensional plate: a periodically constrained elastica under a progressive increase of external forces.

oscillations growing together. They introduced a structural instability created by uniformly distributed external compression that appears to enhance flow instabilities, therefore reducing the flow velocity required to start structural oscillatory motions (see [32,33] for instability analysis of plates under axial forces). Muriel et al. [30] was limited to a proof of concept for energy harvesting, mainly focusing, experimentally, on the optimization of consistent oscillatory behavior and reduction of three-dimensional effects, and Muriel and Cowen [31] experimentally studied the onset of oscillatory behavior of such a structure. Here we report on a reduced model of [30] (i.e., [31]), a single plate under periodic external forcing (Fig. 1 and details in Section 2.1). We study the device experimentally to obtain a second mode deformation, and solve the Newtonian equilibrium equations numerically to predict deformations caused by the nonlinearities induced by kinematic (i.e., geometry) and dynamic (i.e., forces) boundary conditions. Here, the vanishing nature of the later present challenges for commercial finite element codes, as the stiffness matrix becomes singular as a second mode deformation develops. Our experimental results show an elastic bifurcation and buckling instability via periodic external forcing, with locally stabilized first and second mode deformations (the action of a small force causes branch switching when in the second mode). The numerical results show that the model is capable of predicting such modes of deformation, as well as active and inactive constraints as part of the solution to the non-linear problem.

2. Numerical model of the periodically-constrained heavy elastica

In this letter, we limit our discussion to the study of static buckling of a periodically constraint heavy elastica in two dimensions (Fig. 2a). It will serve as a model for our plate by restricting the deflection to only cylindrical bending of the elemental strip, where the flexural rigidity, D, of the unit-width strip ($b = 1$) is $D = EI/(1-\nu^2)$, with E being the Young's modulus, I the area moment of inertia, and ν Poisson's ratio [34].

We consider the elastica to be inextensible of length L_p (non-dimensional $l = 1$), of uniform cross-section, elasticity, density, and thin enough such that the Euler assumption holds (i.e., the total curvature is proportional only to the local moment [35]). Under these assumptions, we look for a strong form formulation.

The conception of such model follows from a straight plate of length L_p, with tension lines of length L_s, δ_p apart, and with connection coordinates (x_p, y_p) (Fig. 2b). The other end of the tension lines are attached to an infinitely rigid frame, with connections spaced δ_f apart at coordinates (x_o, y_o). Originally, the plate hangs straight from the tension lines, which are being strained only by the action of the plate's weight. As we progressively decrease δ_f and keep δ_p constant, different tension lines activate or deactivate (Fig. 2c). On active lines, tension forces H appear, forces which induce a series of deformations as $(\delta_p - \delta_f)/\delta_p$ increases. The tension lines have a net compressive effect on the plate.

2.1. Experimental realization of a second mode buckled plate

We induce a deformation presented in Fig. 1 with a series of tension lines that buckle a plate into a two-dimensional wavelike shape. The plate is made of a single translucent polycarbonate sheet with thickness $\delta = 0.400 \pm 0.007$ mm, length $L_p = 60 \pm 0.05$ cm, width $B = 30 \pm 0.05$ cm, density $\rho_p = 1.14 \pm 0.03$ g/cm^3, and Poisson ratio $\nu = 0.37$. External tension is created using a series of inner tension lines mounted to parallel side-frame lines as seen in Fig. 1. The side-frame lines are made of micro-filament braided line (Spectra®), 0.4 mm in diameter. Similarly, the lines providing the tension are composed of micro-filament with length $L_{ss} = 7.62 \pm 0.05$ cm, separation along the plate of $\delta_p = 2.90 \pm 0.05$ cm, and separation on the side-frame of $\delta_f = 2.45 \pm 0.05$ cm (Fig. 2a). This difference between the two separations (δ_p and δ_f) provides the external tension necessary to induce the plate's deformation (Fig. 2c). $L_s = 2.9 \pm 0.05$ cm on Fig. 2a is the projection of L_{ss} onto a 2-dimensional plane.

External tension is not modified experimentally. A first way to do this is to change L_{ss}, which proves useful on enhancing oscillatory motions of two coupled plates with an internal membrane [for details, see 30]. However, such an approach provides inconsistent oscillatory motions of decoupled plates (i.e., the plate under study). A second option is to modify δ_f as it is done numerically, however, as it will be shown in Section 3, varying δ_f to obtain a second mode deformation is within the experimental uncertainty.

Reasons for the preference of a second mode deformation are threefold, mainly related to the possibility of energy harvesting. First, mass transport was demonstrated leveraging over a second mode deformation by Muriel et al. [30]. Second, such mode is chosen to resemble a hypothesized onset of flapping over flexible

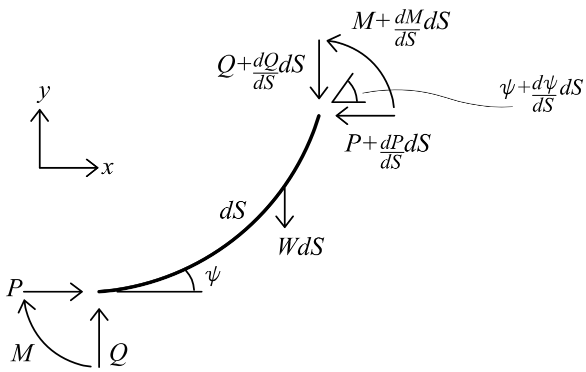

Fig. 3. An elemental segment of the heavy elastica.

plates with high angles of attack (i.e., the order of the deformation is greater than the plate's thickness) as a traveling sinusoidal wave. And third, the higher potential energy compared to first mode, which, after physically realized, transitions into oscillatory motions at low flow velocities as natural oscillatory frequency is reduced [31].

2.2. Equilibrium equations

From Fig. 3, the dimensional equilibrium equations are [35–42]:

$$\begin{aligned} &dX/dS = \cos\psi, && dY/dS = \sin\psi, \\ &d\psi/dS = M/D, && dM/dS = Q\cos\psi - P\sin\psi, \\ &dP/dS = 0, && dQ/dS = -W, \end{aligned} \tag{1}$$

where P and Q are the internal forces parallel to the X and Y axis, M is the internal moment, S is the arc measured from a convenient origin, ψ the angle between the tangent and the horizontal, and W is the weight per unit length.

We define the following non-dimensional parameters:

$$\begin{aligned} &x = X/L_p, && y = Y/L_p, \\ &p = PL_p^2/D, && q = QL_p^2/D \\ &s = S/L_p, && m = ML_p/D, \\ &w = WL_p^3/D, \end{aligned} \tag{2}$$

and we express Eq. (1) in non-dimensional form (Appendix A includes inertial and damping forces for completeness of the model), with $'$ indicating $\partial/\partial s$:

$$\begin{aligned} &x' - \cos\psi = 0, && y' - \sin\psi = 0, \\ &\psi' - m = 0, && m' - q\cos\psi + p\sin\psi = 0, \\ &p' = 0, && q' + w = 0. \end{aligned} \tag{3}$$

2.3. Contact modeling

The heavy elastica is periodically-constrained by a series of tension lines of unstrained length, L_s (Fig. 2a). The area of possible locations of the constrained support is defined by a circle of radius L_s. As not all the supports will be under tension at the same time, we define an active constraint as a support located at the circumference of such circle, and beyond. Active and inactive constraints will be determined as part of the equilibrium solutions of the nonlinear problem.

A tension force, H, appears at the location of active constraints. This force is transmitted to an infinitely rigid support by the tension lines connected to the elemental strip. This connection is considered as passive (i.e., contacts generate no friction, no moment, and no elastic singularity [43]). This implies continuity of angles and moments. We propose the following constitutive relation, mathematically consistent with Hook's law, to model such forces:

$$H = -E_s A_s e, \tag{4}$$

where E_s is the tension lines' Young's modulus, A_s is the area of the unstrained tension line, and e is the engineering strain defined by $e = (l_e - L_s)/L_s$, where l_e is the deformed length of the tension lines. For any $e < 0$, the lines are considered slack, and therefore, no tension is transmitted. This solves the major challenge found with commercial packages, for which the stiffness matrix becomes singular for this condition. The signs give the directionality depicted in Fig. 2b.

H can be decomposed into Cartesian components as follows:

$$H_x = -E_s A_s e\frac{\triangle x}{l_e}, \quad H_y = -E_s A_s e\frac{\triangle y}{l_e}, \tag{5}$$

and by knowing that $\triangle x = x_p - x_o$, $\triangle y = y_p - y_o$, and $l_e = \sqrt{(x_p - x_o)^2 + (y_p - y_o)^2}$, H can be expanded and presented in its nondimensional form as:

$$\begin{aligned} h_x &= -\left(\frac{E_s A_s L_p^2}{D}\right)\frac{\left(\sqrt{(x_p - x_o)^2 + (y_p - y_o)^2} - L_s\right)}{L_s} \\ &\quad \frac{(x_p - x_o)}{\sqrt{(x_p - x_o)^2 + (y_p - y_o)^2}}, \\ h_y &= -\left(\frac{E_s A_s L_p^2}{D}\right)\frac{\left(\sqrt{(x_p - x_o)^2 + (y_p - y_o)^2} - L_s\right)}{L_s} \\ &\quad \frac{(y_p - y_o)}{\sqrt{(x_p - x_o)^2 + (y_p - y_o)^2}}. \end{aligned} \tag{6}$$

2.4. Boundary conditions

The proposed periodically-constrained heavy elastica is subject to the following boundary conditions:

$$\begin{aligned} &m(0) = 0, && m(1) = 0, \\ &p(0) = 0, && p(1) = 0, \\ &q(0) = 0, && q(1) = 0. \end{aligned} \tag{7}$$

2.5. Solutions to the equilibrium equations

We approach the nonlinear problem posed by Eq. (3) and Eq. (6) as a minimization problem of the form:

$$\min \boldsymbol{f}(\boldsymbol{a}) \tag{8}$$

where the objective function $\boldsymbol{f}(\boldsymbol{a})$ is the error function (Eq. SA.11, Eq. SA.17, and Eq. SA.22)[1] formed by discretizing the strong form equations with a second order centered difference scheme Suppl. Mat. A. To solve the minimization problem in Eq. (8), we use the trust-region-dogleg [44] and Levenberg–Marquardt [45–47] algorithms from Matlab® Optimization Toolbox™. A convergence study is presented in Suppl. Mat. C.

To obtain first mode deformations, the initial solution is the trivial plate state (i.e., straight). To obtain second mode deformations, the initial solution is a combination of the experimental

[1] See Supplemental Material at https://doi.org/10.1016/j.eml.2018.03.006 for details on uncertainty analysis, discretization of equations, and convergence study.

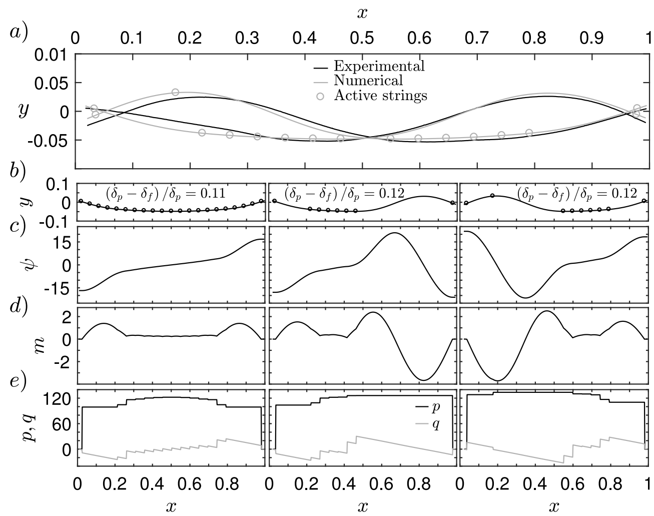

Fig. 4. Results of equilibrium states: (a) Experimental vs numerical second mode deformations. (b) Examples of deformations with their respective (c) angles (ψ), (d) moments (m), and (e) internal forces (p and q). $\|\boldsymbol{f}(\boldsymbol{x})\|^2 = 0$ within machine precision for depicted modes ($\|\ \|$ represents the Euclidean norm).

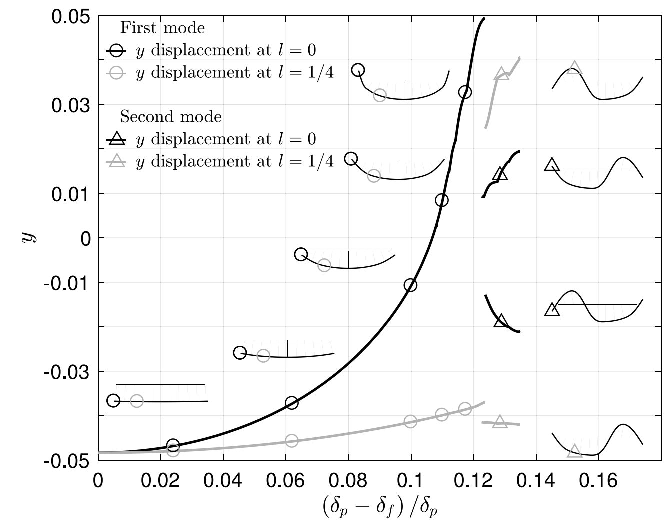

Fig. 5. Bifurcation diagram. $\|\boldsymbol{f}(\boldsymbol{x})\|^2 = 9.7\text{e}{-07}$ for first mode deformations, and $\|\boldsymbol{f}(\boldsymbol{x})\|^2 = 4.1\text{e}{-08}$ for second mode deformations.

deformation and theoretical moments, angles and shear forces of a double pinned elastica Suppl. Mat. C. To obtain additional deformations, δ_f is reduced progressively and the initial solution is the previous obtained deformation.

3. Results and discussion

Experimental results (Figs. 1 and 4a) show that the present configuration represents an elastic bifurcation and buckling instability [48]. It is elastic because the plate immediately returns to the initially straight configuration when external forcing is removed. It is a bifurcation because the equilibrium path bifurcates when the solution looses its uniqueness, showing at least two equilibrium positions. It is an instability because the plate departs from its straight configuration at a critical load value and buckles, experiencing large deformations. Additionally, the two-second mode equilibrium deformations defined by the black lines on Fig. 4a, represent a state of local stability, where small external forces (other than those induced by the tension lines) cause mode branching (snap-through and snap-back). The aforementioned is a similar behavior to that of a double well restoring force potential [49]. Furthermore, first mode equilibrium positions also exist but are not shown, and deformations similar in shape to modes higher than one or two exist but are only momentarily present. Such ephemeral behavior is due to changes in the necessary conditions to realize such higher order modes, specifically, the elongation and tension of the side frames, which relaxes inevitably with time.

The model equations show that compressive forces and the plate's weight always have a destabilizing effect (Eq. (3)). This has important implications on fluid–structure interaction applications, as greater compressive forces will mean lower flow velocities required to initiate structural oscillatory motions. Furthermore, Eqs. (3) and (6) show that the sources of nonlinearities are the geometry, as changes in shape are taken into account to set up the equilibrium equations, and force boundary conditions, as the applied forces by tension lines depend on the plate's deformation. Additionally, special care must be taken with force boundary conditions, as a small strain variation will cause large changes in tension forces (Eq. (4), where H grows rapidly with e). Taking this into consideration when analyzing solutions is important, as infinitesimal variations in displacement (within experimental uncertainty, Suppl. Mat. B) will cause poor convergence.

The results show that the model predicts well the first and second mode deformations (Fig. 4), with $\|\boldsymbol{f}(\boldsymbol{x})\|^2 = 0$ within machine precision ($\|\ \|$ represents the Euclidean norm). A comparison of second mode deformations in Fig. 4a, reveals a close agreement between experimental and numerical results. The inflection points are correctly predicted, and active tension lines (gray circular markers on Fig. 4a) are the result of the numerical analysis. However, a discrepancy in the equilibrium shape is noted, specifically on the first lobe from left to right. This difference can be attributed to experimental uncertainty, where the load parameter $(\delta_p - \delta_f)/\delta_p = 0.155 \pm 0.023$ corresponds to the experimental configuration, and where the respective plotted deformations for comparison are the numerical results of $(\delta_p - \delta_f)/\delta_p = 0.124$, selected to match the location of the boundaries (i.e., $l = 0$ and $l = 1$).

Moreover, Fig. 5 numerically confirms the bifurcation of the solution found experimentally. First mode deformations extend from the trivial equilibrium solution to $(\delta_p - \delta_f)/\delta_p = 0.1234$. The mode with opposite curvature to that of the first mode presented was not found numerically, which is attributed to convergence of the model rather than a statement of non-existence of such a deformation. Additionally, second mode deformations start from $(\delta_p - \delta_f)/\delta_p = 0.1224$ and extends to $(\delta_p - \delta_f)/\delta_p = 0.1348$. On one hand, this range shows an area where first and second mode deformations are possible, confirming the non-uniqueness of the solution. On the other, the range defines the bifurcation region found experimentally, where solutions for second mode deformations coexist. Here, small external forcing other than that provided by tension lines can cause mode branching.

Similarly, the mechanisms available experimentally to transition from first to second mode deformations are infinitesimal perturbations at the bi-stability range or the exceedance of the load parameter at the limit of said range. Infinitesimal perturbations can be provided by intrinsic material non-uniformity, temporally available external forces, or experimental uncertainty of configuration measurements. Independent of the source, perturbations force the plate into a second mode, where the reconfiguration of tension lines provides the local stability necessary to realize such mode. Exceedance of the load parameter causes a similar reconfiguration of active and inactive tension lines, but in this case, the restoring action of bending stiffness is exceeded by no external force other than that of the tension lines. In such deformations, potential energy is a function of strain energy and work done by external forces, and therefore different for different deformation modes. If an external, temporally dependent forcing is considered, the oscillatory mode will depend on the magnitude of such forcing.

Finally, discretization of the model as a strong form, in addition to the algorithms implemented, may be affecting the converge of other modes (e.g., see third deformation from top to bottom on Fig. 2c, or higher order modes), and the completeness of the equilibrium path shown in Fig. 5. While $\|\boldsymbol{f}\,(\boldsymbol{x}\setminus\boldsymbol{h})\|^2 = 0$ (with $\setminus$ indicating relative complement) within machine precision, $\|\boldsymbol{f}\,(\boldsymbol{h})\|^2$ presents unacceptable errors in terms of convergence. This is closely related to the rapid change of tension forces as a function of strain. For example, a discrepancy of 10 µm accounts for a changes in h of the same magnitude as that of internal forces presented in Fig. 4. While this error is unacceptable numerically, 10 µm is far bellow experimental uncertainty.

4. Final remarks

We presented the study of a periodically constrained plate, induced into a second mode deformation. Experimentally, buckling instability and elastic bifurcation of second mode deformations with snap-through and snap-back are self-evident. Numerical results based on a two-dimensional periodically constrained heavy elastica corroborate experimental findings, and point towards the possibility of multiple equilibrium solutions, where first and second mode deformations are solutions for a single control parameter $\left(\delta_p - \delta_f\right)/\delta_p$. Results show good convergence, but sensitivity of tension force components, h_x and h_y, represents difficulties in finding the full equilibrium path and other possible equilibrium positions with shapes resembling higher order modes. To resolve this, the implementation of the slack condition presented in Section 2.3 could be implemented based on a Hamiltonian derivation.

Work remains on stability analysis, large and small vibrations, and coupling with fluids as part of the larger scope of the problem, for which the deformation was originally conceived. On these topics, extensive studies have been conducted on plates (see [50,32,51,52] and references therein). The use of external forcing, first to induce a departure from trivial stability into a buckling instability, and at the same time to locally stabilize second mode deformations, has larger implications on fluid–structure interaction problems: the use of such deformations can prove useful in reducing critical flow velocities to start structural oscillations, and increasing operational range of such applications [32,33].

Acknowledgments

We want to thank Professor Christopher Earls for valuable conversations that lead to some of the ideas presented herein, and Professor Peter Thomson for fruitful discussions on structural stability. We gratefully acknowledge the support of the DeFrees Family through the DeFrees fellowship, as well as the David R. Atkinson Center for a Sustainable Future at Cornell University and the Colombian National Science Foundation (Colciencias) for their financial support. Any opinions and comments are those of the authors and do not necessarily reflect the views of the sponsors. The authors have no competing interests to declare.

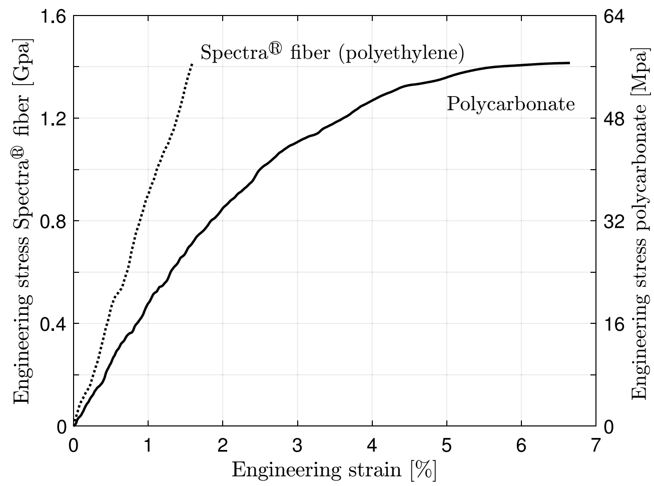

Fig. B.6. Polycarbonate and Spectra® fiber tensile modulus.

Appendix A. Equilibrium equations with inertial and damping terms

By including inertial and damping terms, Eq. (1) becomes [53]:

$$\begin{aligned}
&\partial X/\partial S = \cos\psi,\\
&\partial Y/\partial S = \sin\psi,\\
&\partial \psi/\partial S = M/D,\\
&\partial M/\partial S = Q\cos\psi - P\sin\psi,\\
&\partial P/\partial S = -\left(W/g\right)\partial^2 X/\partial T^2 - C\partial X/\partial T,\\
&\partial Q/\partial S = -W - \left(W/g\right)\partial^2 Y/\partial T^2 - C\partial Y/\partial T,
\end{aligned} \tag{A.1}$$

where T is the dimensional time, and C is the damping coefficient.

We define the additional non-dimensional parameters:

$$t = T/L_p^2\sqrt{(Dg/W)}, \quad c = CL_p^2\sqrt{(g/WD)}. \tag{A.2}$$

We express Eq. (A.1) in non-dimensional form:

$$\begin{aligned}
&\partial x/\partial s = \cos\psi,\\
&\partial y/\partial s = \sin\psi,\\
&\partial \psi/\partial s = m,\\
&\partial m/\partial s = q\cos\psi - p\sin\psi,\\
&\partial p/\partial s = -\partial^2 x/\partial t^2 - c\partial x/\partial t,\\
&\partial q/\partial s = -w - \partial^2 y/\partial t^2 - c\partial y/\partial t,
\end{aligned} \tag{A.3}$$

which can be used to extract the non-dimensional equilibrium equations, or explore small and large vibrations.

Appendix B. Elastic modulus for polycarbonate and microfilament braided line

Fig. B.6 reports the tensile modulus for the polycarbonate plate and Spectra® fiber (polyethylene) used for the experimental model presented in Fig. 1, with details in 2.1. The experimental procedure for polycarbonate and fibers followed [54] and [55] respectively. Modulus for the plate and the fiber are $E = 1.97 \pm 0.04$ GPa and $E_s = 88.9 \pm 2.43$ GPa, respectively (see Suppl. Mat. B for uncertainty analysis details).

Appendix C. Supplementary data

Supplementary material related to this article can be found online at https://10.1016/j.eml.2018.03.006.